

# Structural behaviour of copper chloride catalysts during the chlorination of CO to phosgene†

Shaoliang Guan,<sup>id</sup> <sup>ab</sup> Philip R. Davies,<sup>id</sup> <sup>a</sup> Emma K. Gibson,<sup>id</sup> <sup>ce</sup> David Lennon,<sup>\*b</sup> Giovanni E. Rossi,<sup>b</sup> John M. Winfield,<sup>b</sup> June Callison,<sup>c</sup> Peter P. Wells,<sup>id</sup> <sup>cdf</sup> and David J. Willock<sup>id</sup> <sup>\*a</sup>

Received 15th January 2018, Accepted 16th January 2018

DOI: 10.1039/c8fd00005k

The interaction of CO with an attapulgite-supported Cu(II)Cl<sub>2</sub> catalyst has been examined in a micro-reactor arrangement. CO exposure to the dried, as-received catalyst at elevated temperatures leads to the formation of CO<sub>2</sub> as the only identifiable product. However, phosgene production can be induced by using a catalyst pre-treatment where the supported Cu(II)Cl<sub>2</sub> sample is exposed to a diluted stream of chlorine. Subsequent CO exposure at ~370 °C then leads to phosgene production. In order to investigate the origins of this atypical set of reaction characteristics, a series of X-ray absorption experiments were performed that were supplemented by DFT calculations. XANES measurements establish that at the elevated temperatures connected with phosgene formation, the catalyst is comprised of Cu<sup>+</sup> and a small amount of Cu<sup>2+</sup>. Moreover, the data show that unique to the chlorine pre-treated sample, CO exposure at elevated temperature results in a short-lived oxidation of the copper. On the basis of calculated CO adsorption energies, DFT calculations indicate that a mixed Cu<sup>+</sup>/Cu<sup>2+</sup> catalyst is required to support CO chemisorption.

## Introduction

There is a rapidly increasing demand for polyurethanes as lightweight, robust and transparent components in manufacturing. These polymers are prepared from

<sup>a</sup>Cardiff Catalysis Institute, School of Chemistry, Cardiff University, Cardiff, CF10 3AT, UK. E-mail: willockdj@Cardiff.ac.uk

<sup>b</sup>School of Chemistry, University of Glasgow, Joseph Black Building, University Avenue, Glasgow, G12 8QQ, UK. E-mail: david.lennon@glasgow.ac.uk

<sup>c</sup>UK Catalysis Hub, RCaH, Rutherford Appleton Laboratory, Didcot, OX11 0FA, UK

<sup>d</sup>Diamond Light Source Ltd., Diamond House, Harwell Science and Innovation Campus, Didcot, Oxfordshire OX11 0DE, UK

<sup>e</sup>Department of Chemistry, University College London, Gordon Street, London, WC1H 0AJ, UK

<sup>f</sup>School of Chemistry, University of Southampton, Southampton, SO17 1BJ, UK

† Electronic supplementary information (ESI) available. See DOI: 10.1039/c8fd00005k



isocyanates with methylene diphenyl diisocyanate being a representative material. Methylene diphenyl diisocyanate is itself prepared through the phosgenation of 4,4'-methylenedianiline, for which the total global production capacity in 2010 was estimated to be 5 million tonnes.<sup>1</sup> Consequently, there is a high global demand for phosgene. Typically, phosgene production is undertaken alongside isocyanate production facilities as part of an integrated chemical complex. Chlorine, as a component of phosgene, is a major feedstock in the process but no chlorine is incorporated into the isocyanate product; it all ends up as HCl which represents a significant burden to the manufacturer and the environment.<sup>1</sup> Cavani has previously considered routes by which the chlorine cycle in certain chemical industry operations could be made more efficient by means of the direct use of HCl as a co-reactant in oxychlorination reactions.<sup>2</sup> More specifically, Zhang and co-workers have described how the oxychlorination of carbon monoxide may be exploited to produce phosgene.<sup>3–5</sup> In order to effect sufficient separation of reagents/products, Zhang *et al.* propose a three stage process in which the first stage involves the chlorination of CO to produce phosgene over a supported copper(II) chloride catalyst whilst simultaneously reducing the catalyst to copper(I) chloride (Cu(I)Cl).

Despite the potential of an oxychlorination process cycle capable of producing phosgene whilst consuming the HCl by-product of isocyanate manufacturing, there is a paucity of data on the surface chemistry of this process. This communication will examine aspects of the surface chemistry exclusively associated with the first stage of the oxychlorination cycle outlined by Zhang *et al.*, namely the interaction between CO and a supported Cu(II)Cl<sub>2</sub> catalyst. In an attempt to concentrate on durable materials, an industrial grade attapulgite supported Cu(II) Cl<sub>2</sub> catalyst is examined. This catalyst has previously been investigated for the manufacture of trichloroethene and tetrachloroethene.<sup>6,7</sup> (Attapulgite is the mineralogical name for palygorskite, a porous material formed from interspersed sheets of silica and sheets of octahedrally co-ordinated cations drawn from Mg<sup>2+</sup>, Al<sup>3+</sup> and Fe<sup>3+</sup>.<sup>8,9</sup>)

Related materials such as Cu(II)Cl<sub>2</sub>/γ-Al<sub>2</sub>O<sub>3</sub>, which finds applications in the synthesis of the vinyl chloride monomer *via* the oxychlorination of ethene, have been studied using a range of techniques including UV/Vis, XANES and EXAFS.<sup>10,11</sup> These studies have identified at least two distinct Cu species, at low loadings (<2%) Cu is found to be accommodated in surface sites on the alumina support with no Cl<sup>−</sup> in the first co-ordination sphere.<sup>12</sup> These species show EPR signals with axial symmetry. The Cl<sup>−</sup> released from the CuCl<sub>2</sub> appears as surface Al–Cl species. At higher loadings a second Cu species appears with Cu–Cl bonds present. This secondary species is found to be soluble in ethanol and the material loaded in this way leads to a more complex EPR spectrum. EXAFS measurements on the high loading samples show that Cu<sup>2+</sup> is reduced in the presence of the ethene reagent.<sup>13</sup> It was also suggested that KCl can act to stabilise Cu(II)Cl<sub>2</sub>, making the reduction processes more challenging and switching the rate determining step for dichloroethane production from Cu(I)Cl oxidation to Cu(II)Cl<sub>2</sub> reduction by ethene.<sup>14</sup>

Respecting the theme of this Faraday Discussion meeting, this paper will concentrate on how a specific catalyst pre-treatment is able to facilitate favourable CO turnovers, in this case for the synthesis of phosgene. After a preliminary consideration of phosgene production in the presence of an as-received Cu(II)Cl<sub>2</sub>



catalyst and a Cu(II)Cl<sub>2</sub> catalyst that has been pre-treated with dichlorine, the paper adopts a two-strand approach to address the detailed structural and oxidation state changes that occur as CO interacts with the supported Cu(II)Cl<sub>2</sub> material. Firstly, a series of synchrotron X-ray absorption (XAS) experiments will be described that provide information on oxidation states and structure. Secondly, and on the basis of the XAS measurements, a series of DFT calculations are presented that explore possible structural motifs and energetics of the interaction between CO and Cu(II)Cl<sub>2</sub>. A follow-up paper will describe the reaction chemistry involved in this complex, but technically relevant, reaction system more comprehensively.<sup>15</sup> The relevance of the catalyst pre-treatment stage to phosgene production is described in the results and discussion section.

Previous work using DFT to study the surface chemistry of related structures has employed the DFT+U approach to account for the strongly correlated nature of electrons at cationic Cu centres. For example, Lebernegg *et al.*<sup>16</sup> have considered magnetic coupling between Cu<sup>2+</sup> centres in copper halides, CuX<sub>2</sub> structures (X = F, Cl, Br), which all form edge sharing linear chains of square planar complexes as described for Cu(II)Cl<sub>2</sub> in the experimental section below. In the calculations presented here we also use a DFT+U approach and include the effect of the *U* parameter on the calculated properties of interest for catalysis.

## Experimental

### Chemicals and materials

CuCl<sub>2</sub> (Sigma-Aldrich, 97%), CuCl<sub>2</sub>·H<sub>2</sub>O (Sigma-Aldrich, 99.99%), CuO (Acros Organics, 97%) and Cu<sub>4</sub>(OH)<sub>6</sub>Cl<sub>2</sub> (Supelco, ≤100%) were used as received. The catalyst supplied by Ineos Chlor Ltd. contains 10% CuCl<sub>2</sub> and 8% KCl supported on an attapulgite clay and is described elsewhere.<sup>6,7</sup> Before use the material was dried under a continuous stream of N<sub>2</sub> (BOC, 99.998%) at a flowrate of 50 mL min<sup>-1</sup> and a temperature of 110 °C for 12 h. Chlorine pre-treated catalyst samples were prepared by exposing the dried catalyst to a Cl<sub>2</sub>/N<sub>2</sub> co-feed (6 mL min<sup>-1</sup> Cl<sub>2</sub>, 50 mL min<sup>-1</sup> N<sub>2</sub>) for 10 min at 370 °C. This chlorine exposure was repeated a further three times before reverting the carrier gas back to pure N<sub>2</sub>. The sample was maintained at 370 °C for 30 minutes, after which the heating was turned off and the sample allowed to cool to ambient temperature in the presence of flowing nitrogen. For the XAS measurements, the dried and chlorine pre-treated copper chloride catalyst samples were isolated in a nitrogen atmosphere for transportation to the synchrotron.

Reaction testing was performed using a micro-reactor facility located at the University of Glasgow. A detailed description of that apparatus will appear in a subsequent publication.<sup>15</sup> Briefly, a combination of in-line UV-visible spectroscopy and infrared spectroscopy was used to monitor the gas phase exiting the reactor.

### Catalyst testing

Reactions were carried out using a flow reactor charged with varying amounts of catalyst (~0.500 g). A by-pass reactor positioned alongside the principal reactor within the furnace was loaded with a comparable mass of ground quartz. All experiments were carried out with an overall flow rate of 159 sccm (standard cubic



centimetre per minute,  $\text{cm}^3 \text{min}^{-1}$ ) in order to keep the contact time the same for all experiments. All gas flows were controlled by using mass flow controllers (Hastings GFC-202, 0–100 sccm). In order to avoid corrosion, an  $\text{N}_2$  purge system was connected to the mass flow controllers to ensure the lines were purged when not in use.

Reagent gases were mixed in a mixing vessel with Ballotini balls to ensure dispersion of the gases, followed by an in-line filter to retain catalyst particles in the reactor. The reaction temperature was monitored using a thermocouple (HANNA HI 93532) with a probe in the sleeve of the reactor loaded with the catalyst. Post-reactor, an  $\text{N}_2$ -drive line feeds into the flow before a second in-line filter; this arrangement ensures that all reagents remain in the gaseous phase. A three-way valve allows the reactor exit flow to be directed either to the IR and UV-Vis spectrophotometers or directly through a chemical scrubber to the vent. The scrubber was filled with an aqueous solution of NaOH that ensured the chlorinated products were neutralised before exiting *via* the vent.

### XAFS

Copper K-edge XAFS studies of the catalyst materials and a series of reference standards were carried out on the B18 beamline at the Diamond Light Source, Didcot, UK. Measurements were performed using a quick extended (QE) XAFS setup with a fast-scanning silicon (111) double-crystal monochromator. The time resolution of the spectra reported herein was 49 seconds per spectrum ( $k_{\text{max}} = 14$ ), and on average three scans were acquired to improve the signal-to-noise ratio of the data. All *ex situ* samples were diluted with cellulose to optimize the effective-edge step of the XAFS data and measured in transmission mode using ion-chamber detectors. Reference samples were  $\text{CuO}$ ,  $\text{CuCl}_2$ ,  $\text{CuCl}_2 \cdot \text{H}_2\text{O}$ , and  $\text{Cu}_4(\text{OH})_6\text{Cl}_2$ . A reference spectrum of anhydrous  $\text{CuCl}_2$  was prepared *in situ* by heating  $\text{CuCl}_2$  (Sigma Aldrich 99.995%, with boron nitride) in a 3 mm O.D. quartz capillary under flowing helium. After reaching  $100^\circ\text{C}$  the XANES spectra resembled that reported earlier by Ferrandon *et al.*<sup>17</sup> All transmission XAFS spectra were acquired concurrently with the copper reference foil placed between  $I_t$  and  $I_{\text{ref}}$  XAS data processing, and EXAFS analysis was performed using IFEFFIT<sup>18</sup> with the Horae package<sup>19</sup> (Athena and Artemis).

*In situ* XAFS measurements were performed in transmission mode using a fixed-bed quartz microreactor (O.D. 5.6 mm, length 200 mm, Hilgenberg), with a gas flow setup similar to that described by Matla *et al.*<sup>20</sup> Due to the high loading of Cu in the catalyst the samples were mixed with boron nitride to achieve an optimal absorption in the XAFS spectra. The temperature was controlled using a Eurotherm controller with a type K thermocouple positioned in the centre of the heater block. The reactor was heated to  $370^\circ\text{C}$  at a ramp rate of  $10^\circ\text{C min}^{-1}$  under a flow of He ( $50 \text{ mL min}^{-1}$ , 99.99% BIP, BOC). The reactor was then held at this temperature for 30 min under a flow of CO in He ( $50 \text{ mL min}^{-1}$ , 10% CO in He). Finally, the reactor was cooled down to room temperature under He.

### Density functional theory

All calculations were carried out using the VASP package<sup>21</sup> with the PBE functional.<sup>22</sup> Core states for all atoms were represented using the projector augmented wave (PAW) method.<sup>23</sup> The PAW potentials for Cu and Cl left 11 and 7 electrons in



the valence states for the respective neutral atoms, while all other atoms have their expected number of valence electrons.

The crystal structure of  $\text{Cu}(\text{n})\text{Cl}_2$  is shown in Fig. S1.† The material has a layered structure with  $\text{Cu}^{2+}$  cations in rows of edge sharing square planar structures aligned with the  $b$ -axis of the unit cell. Neighbouring  $\text{Cu}^{2+}$  ions are bridged by two co-ordinated  $\text{Cl}^-$  anions. The rows are arranged to give each  $\text{Cu}^{2+}$  ion an additional two axial  $\text{Cl}^-$  ligands in neighbouring chains. This leads to an experimental crystal structure for anhydrous  $\text{Cu}(\text{n})\text{Cl}_2$  in which each  $\text{Cu}^{2+}$  cation has 4 short Cu–Cl (2.35 Å) and 2 long Cu–Cl distances (2.9 Å), so that the  $\text{Cu}^{2+}(\text{d}^9)$  centres can be thought of as having a strongly Jahn–Teller distorted environment. Besides this weak axial co-ordination between  $\text{Cu}^{2+}$  and  $\text{Cl}^-$ , inter-row and inter-layer spacing is dependent on dispersion interactions and so all calculations included a parameterised representation of the dispersion interaction using the Grimme D2 approach.<sup>24</sup> We use reciprocal space ( $k$ -point) sampling following the Monkhorst–Pack scheme.<sup>25</sup> Convergence of the bulk energy for  $\text{Cu}(\text{n})\text{Cl}_2$  with respect to planewave cutoff and  $k$ -point sampling was tested (Fig. S2†) resulting in a planewave cutoff of 500 eV and  $k$ -point sampling of  $5 \times 5 \times 5$  for the bulk unit cell. For density of states (DOS) calculations the density of the  $k$ -point sampling was increased to  $7 \times 7 \times 7$ . The  $k$ -point sampling was adjusted for the larger unit cells used to represent surfaces to  $3 \times 3 \times 1$  with only 1  $k$ -point used in the direction perpendicular to the surfaces of slab models. A check of the calculated surface defect energy using  $5 \times 5 \times 1$   $k$ -point sampling showed a variation of only 0.003 eV. A dipole correction perpendicular to the surface plane was used for all slab calculations.

In addition, as discussed in the introduction section, the strong correlation effects for electrons located at the Cu sites require the application of the DFT+U approach.<sup>26</sup> From analysis of the calculated electronic structure Lebernegg *et al.*<sup>16</sup> suggested that  $\text{Cu}(\text{n})\text{Cl}_2$  can be described using a Hubbard model with  $U_{\text{eff}} = 4.0$ . However, they also point out that differences in local basis set and planewave approaches require higher  $U$  values when calculations are carried out with VASP. More extensive computational literature is available for  $\text{Cu}^{2+}$  and  $\text{Cu}^+$  in oxide materials, due to the promising combination of transparency and electrical conductivity for  $\text{Cu}^+$  containing oxides. Scanlon *et al.*<sup>27</sup> have considered p-type defects in  $\text{Cu}_2\text{O}$  with the PBE functional and found that a  $U$  value of 5.2 best reproduced the valence band features expected from X-ray photoelectron spectroscopy. However, they also concluded that the DFT+U approach cannot reproduce the detailed electronic structure of polaronic defects in this material. Mishra *et al.*<sup>28</sup> have applied DFT+U calculations to study the surface structure and adsorption of  $\text{CO}_2$  to both  $\text{CuO}$  and  $\text{Cu}_2\text{O}$ . They employed a range of  $U$  values and identified  $U = 7$  as giving the best match to the experimental band gap and ion magnetic moments for  $\text{CuO}$ . While the electronic structure of  $\text{Cu}_2\text{O}$  was found to be more challenging,  $U = 7$  was found to give a good account of the geometric structure of the material. In this work we have also looked at the effect of the  $U$  parameter on the calculated energetics through a comparison of results for values of  $U = 4$  and  $U = 7$ , and this allows us to show the sensitivity of the calculated material properties to the choice of this parameter.

The  $\text{d}^9$  configuration of the  $\text{Cu}^{2+}$  centres leads to magnetic interactions between Cu centres which have previously been studied in some detail.<sup>16</sup> We have tested the magnet ordering in the bulk unit cell. This unit cell contains two  $\text{Cu}^{2+}$



ions within each row and two rows of  $\text{CuCl}_2$  (Fig. S1†). We find that having parallel spins at adjacent Cu centres within a  $\text{CuCl}_2$  row is favoured by 0.01 eV per atom but the coupling between rows is much weaker with practically no difference between Cu atoms on adjacent rows having a ferromagnetic or anti-ferromagnetic alignment. The spin arrangement used in our calculations is illustrated in Fig. S3.†

For surface calculations we use a four layer slab model with the lowest layer of  $\text{CuCl}_2$  chains frozen at bulk positions to represent the constraint of the surface matching to a more extended crystal bulk.

The surface energy is calculated with the fixed lower layer taken into account using:<sup>29</sup>

$$E_{\text{surf}}^{\text{opt}} = \frac{E_{\text{slab}} - nE_{\text{bulk}}}{S} - E_{\text{surf}}^{\text{term}} \quad (1)$$

where  $E_{\text{slab}}$  is the energy of the slab calculated with a fixed region at the bottom of the slab and a geometry optimised region for the upper surface. The slab has a surface area,  $S$ , and contains  $n$  stoichiometric units of the bulk cell composition for which the calculated energy is  $E_{\text{bulk}}$ .  $E_{\text{surf}}^{\text{term}}$  is the calculated surface energy for the slab without geometry optimisation, in this case the two sides of the slab are equivalent and so  $E_{\text{surf}}^{\text{term}}$  can be obtained using:

$$E_{\text{surf}}^{\text{term}} = \frac{E_{\text{slab}}^{\text{fixed}} - nE_{\text{bulk}}}{2S} \quad (2)$$

where  $E_{\text{slab}}^{\text{fixed}}$  is the calculated energy for the slab without relaxation of the ionic positions.

The adsorption energy,  $E_{\text{ads}}$ , of CO to the Cu sites of various slab models of the surface were calculated using:

$$E_{\text{ads}} = E_{\text{CO+slab}} - E_{\text{slab}} - E_{\text{CO}} \quad (3)$$

where  $E_{\text{CO+slab}}$  is the energy for the geometry optimised structure with the CO molecule at its adsorption site,  $E_{\text{slab}}$  is the geometry optimised energy of the slab alone and  $E_{\text{CO}}$  is the energy of an optimised structure of CO in the gas phase using the same periodic boundary conditions as for the slab model. In all slab calculations the lowest lying  $\text{CuCl}_2$  chains were frozen at their bulk co-ordinates as described for surface energy calculations.

## Results and discussion

The FT-IR spectra of the products resulting from CO reacting with the as-received catalyst (Fig. 1a) indicated that, as well as the signal of unreacted  $\text{C}\equiv\text{O}$  observed at  $2140\text{ cm}^{-1}$ , there is a large peak at  $2343\text{ cm}^{-1}$  due to the asymmetric  $\text{C}=\text{O}$  stretching mode of  $\text{CO}_2$ . The bending mode of  $\text{O}=\text{C}=\text{O}$  at  $660\text{ cm}^{-1}$  can also be seen in the spectra. Importantly, no phosgene formation was observed for the as-received catalyst reacting with CO. A variety of sample conditioning steps were explored but no combination of heating pre-treatments was able to induce phosgene production on CO exposure from this industrial grade  $\text{Cu(II)Cl}_2$  oxy-chlorination catalyst. In contrast, a chemical pre-treatment using short exposures of diluted chlorine (see experimental section), was able to induce phosgene



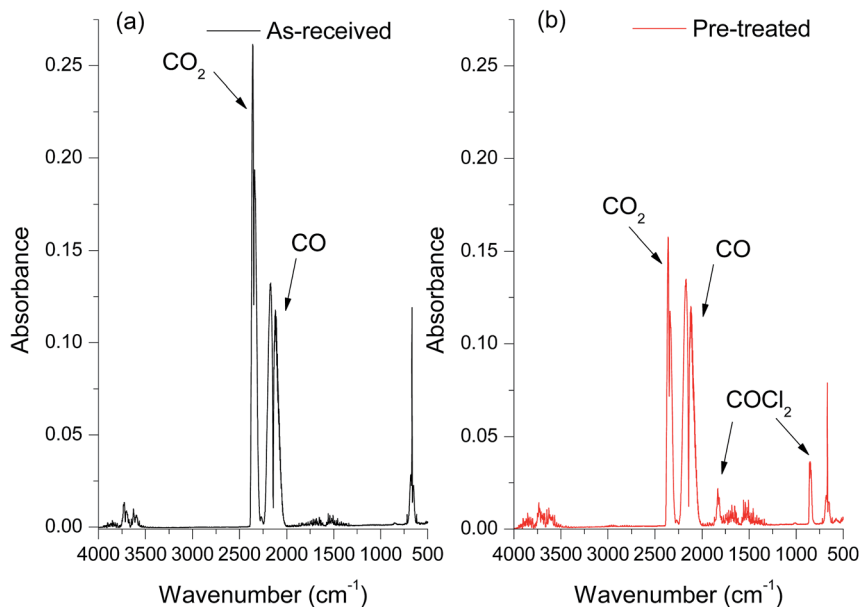


Fig. 1 In-line FT-IR spectra of outlet gas mixture of CO reacting with the catalyst at 370 °C showing the effect of pre-treating the catalyst with  $\text{Cl}_2(\text{g})$ . (a) As-received catalyst; (b) chlorine pre-treated catalyst.

synthesis. Fig. 1b shows the infrared spectrum of the reactor output for CO exposure to a chlorine pre-treated catalyst maintained at 370 °C. In addition to the CO and  $\text{CO}_2$  bands evident in Fig. 1a, bands observed at 1825 and 845  $\text{cm}^{-1}$  are due to the C=O stretch and C-Cl asymmetric stretch in  $\text{COCl}_2$ , respectively. Comparing the two spectra confirms the necessity of a  $\text{Cl}_2$  pre-treatment to the catalyst for phosgene production. Moreover, the attenuation of the  $\text{CO}_2$  band intensity for the chlorine pre-treated catalyst (Fig. 1b) compared to the as-received catalyst (Fig. 1a) suggests that the CO oxidation to produce  $\text{CO}_2$  and CO chlorination to produce  $\text{COCl}_2$  are competing reaction pathways. Importantly, phosgene production cannot be sustained on continued CO exposure. The time dependant characteristics of  $\text{COCl}_2$  and  $\text{CO}_2$  formation is beyond the scope of the present communication and will be more comprehensively examined in a subsequent publication.<sup>15</sup>

To investigate the differences between the as received and  $\text{Cl}_2$  pre-treated material in more detail we turned to XANES measurements. The  $\text{Cu}^+$  or  $\text{Cu}^{2+}$  oxidation states show a number of characteristic features in the XANES region of the Cu K-edge XAFS spectra and a series of reference materials were examined to support the analysis, Fig. 2 (left frame). All of the  $\text{Cu}^{2+}$  reference compounds show a weak pre-edge feature at 8977 eV, due to the  $1s \rightarrow 3d$  transition. This is forbidden for  $\text{Cu}^+$  species.<sup>30</sup> Apart from the pre-edge feature, Kau *et al.*<sup>31</sup> observed no other significant peaks below 8985 eV for any  $\text{Cu}^{2+}$  species. However, for  $\text{Cu}^+$  species, a sharp feature below the dashed line in Fig. 2 would be expected, around 8983 eV due to the  $1s \rightarrow 4p$  transition, this is evident in the spectra for the  $\text{Cu}_2\text{O}$  materials shown in Fig. 2 (right frame).<sup>30</sup>



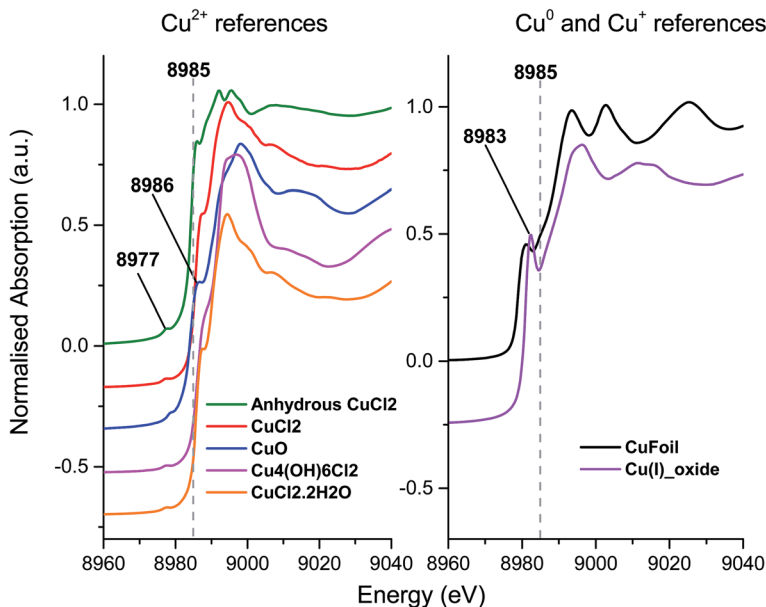


Fig. 2 *Ex situ* XANES spectra – Left:  $\text{Cu}^{2+}$  reference compounds, and right:  $\text{Cu}^+$  reference compounds, spectra are vertically offset for clarity.

The XANES spectra, shown in Fig. 3, of the as-received and  $\text{Cl}_2$  pre-treated catalysts are both consistent with  $\text{Cu}^{2+}$  species, exhibiting the characteristic features at 8986 eV and 8977 eV and without the strong feature at 8983 eV associated with  $\text{Cu}^+$ . The chlorine pre-treated sample resembles that of anhydrous  $\text{CuCl}_2$ , which may imply that the  $\text{Cl}_2$  pre-treatment has, to some extent, driven off adsorbed water or hydroxyl groups from the  $\text{Cu(II)Cl}_2$  catalyst.

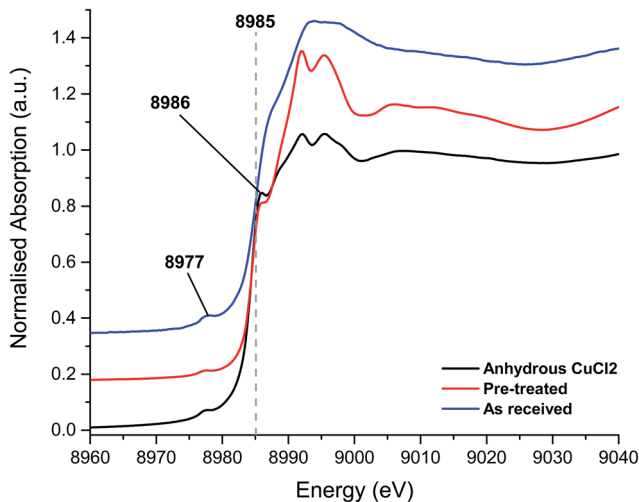


Fig. 3 XANES spectra – fresh catalyst as received, chlorine pre-treated and the anhydrous  $\text{CuCl}_2$  (prepared *in situ*).





On heating the chlorine pre-treated sample from RT to 200 °C the sample initially resembles anhydrous  $\text{CuCl}_2$ , but by 300 °C, the  $1s \rightarrow 3d$  feature at 8977 eV and the feature at 8986 eV consistent with  $\text{Cu}^{2+}$  species loses intensity (Fig. 4). By 360 °C the edge has shifted to lower energy and a pronounced pre-edge feature at 8983 eV is observed, consistent with the presence of a  $\text{Cu}^+$  species. The small feature at 8978 eV is still present, (more easily observed in the 1<sup>st</sup> derivative spectrum, Fig. S4†). We therefore conclude that by the end of the temperature ramp at 367 °C, which corresponds to the temperature at which phosgene production is obtained (Fig. 1b), the sample consists of a mixture of  $\text{Cu}^+$  and a small amount of  $\text{Cu}^{2+}$ . This reduction to  $\text{Cu}^+$  is also observed for the fresh catalyst.

Fig. 5 shows that, after the heating ramp and exposure of the  $\text{Cl}_2$  pre-treated sample to CO (1 min), the characteristic  $\text{Cu}^+$  feature at 8983 eV significantly diminishes in intensity, the adsorption edge shifts to higher energy, and the first feature after the edge (at 8992 eV) increases. In addition, the small pre-edge feature of  $\text{Cu}^{2+}$  at 8977 eV increases, more easily observed in the insert of Fig. 5a. This pre-edge feature, unique to  $\text{Cu}^{2+}$  species, becomes visible on introduction of CO and then disappears almost completely after 10 min of exposure. Although CO is well known as a reducing agent, these changes point unambiguously to an oxidation of  $\text{Cu}^+$  to  $\text{Cu}^{2+}$  during the first minute of CO exposure. Interestingly, this re-oxidation is not observed for the fresh catalyst (Fig. 5b).

From 10 min to 30 min of CO exposure, the spectra resemble  $\text{Cu}^+$  species, with an increasing intensity of the feature at 8983 eV.

The observations on Cu oxidation state from this series of experiments is summarised in Scheme 1: for the  $\text{Cl}_2$  pre-treated catalyst, at the end of the ramp we have a mixture of  $\text{Cu}^+$  and  $\text{Cu}^{2+}$  then, on introduction of CO, re-oxidation occurs giving  $\text{Cu}^{2+}$ , which is quickly reduced to  $\text{Cu}^+$  after 10 min exposure. The oxidation of  $\text{Cu}^+$  to  $\text{Cu}^{2+}$  on introduction of CO to the gas feed is difficult to justify.

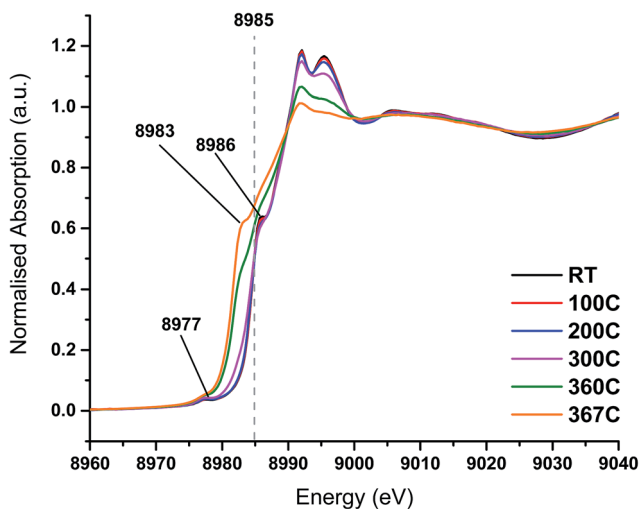


Fig. 4 *In situ* XANES spectra – temperature ramp of chlorine pre-treated catalyst showing loss of anhydrous-like  $\text{Cu}^{2+}$  to  $\text{Cu}^+$  species.



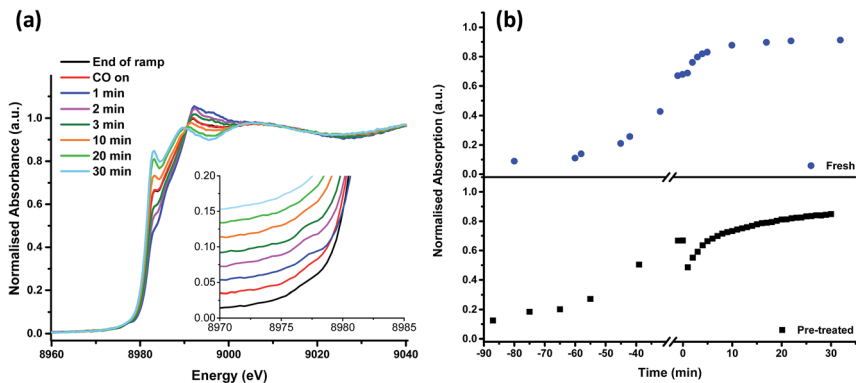
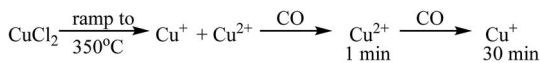


Fig. 5 *In situ* XANES spectra – (a) from the end of the temperature ramp (367 °C, under helium) then on exposure to CO. The insert shows the pre-edge region around 8977 eV in more detail. (b) The time dependence of the pre-edge feature at 8983 eV, characteristic of Cu<sup>+</sup> species during the ramp and on exposure to CO, (blue dots: fresh catalyst, black squares: Cl<sub>2</sub> pre-treated catalyst). Negative time points represent the temperature ramp; time *t* = 0 indicates the time that the catalyst was exposed to CO (temperature = 367 °C).



Scheme 1 A representation of the copper oxidation states accessible to the chlorine pre-treated catalyst on (i) thermal ramping to 350° in a flowing stream of He, (ii) initial exposure to a flowing mixture of He + CO at 367 °C and (iii) extended exposure to a flowing mixture of He + CO at 367 °C.

We speculate that excess chlorine adsorbed within the pore network of the Cl<sub>2</sub> pre-treated material is released when CO is first introduced, and it is this Cl<sub>2</sub> that oxidises Cu. Interestingly, this re-oxidation step is not observed for the fresh catalyst, which only produces CO<sub>2</sub>, whereas the pre-treated catalyst produces both CO<sub>2</sub> and COCl<sub>2</sub> (Fig. 1). Further work is required to better understand the origins of the oxidation process revealed in Fig. 5b.

## EXAFS

Analysis of the extended X-ray absorption fine structure (EXAFS) region was performed on the spectrum after 1 min of CO exposure Fig. 6, Table 1. This corresponds to the conditions under which a maximum in the rate of phosgene production is observed. The magnitude component of the *k*<sup>2</sup> weighted Fourier transform of the data of the spectra recorded at 1 min of CO exposure, Fig. 6, hint that a low *Z*-number scatterer is present. This is similar to the work of Lamberti *et al.*<sup>32</sup> who propose a mixture of copper aluminate and active CuCl<sub>2</sub> in their CuCl<sub>2</sub>/Al<sub>2</sub>O<sub>3</sub> catalyst. Our data fits well to Cu–O and Cu–Cl contributions at 1.84 ± 0.02 and 2.21 ± 0.01 Å, respectively, in Fig. 6 and Table 1. From the XANES spectrum after 1 min of CO exposure (Fig. 5a), we expect the Cu to exist in a distorted octahedral environment, however, the refined coordination numbers from the EXAFS analysis are lower than expected. There are two possibilities to explain



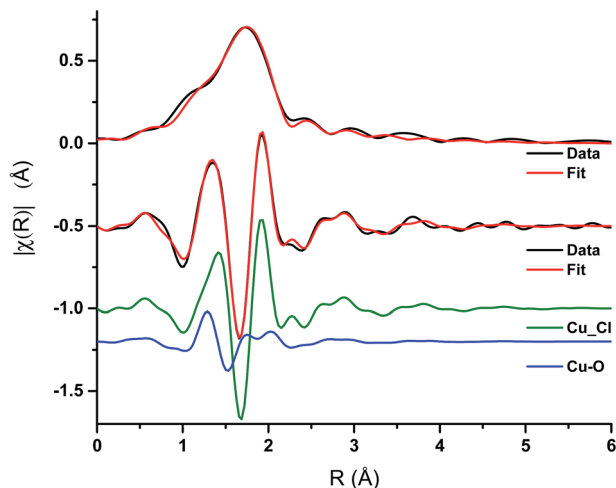


Fig. 6 EXAFS spectra – magnitude component of the  $k^2$  weighted Fourier transform of the data and fit for the 1 min CO exposure spectrum, and the imaginary component of the paths used in the fit.

Table 1 EXAFS fitting parameters,  $S_0^2 = 0.9$ , as determined by the use of a Cu foil standard. Fit range  $3.3 < k < 10.1$ ,  $1 < R < 3$ ; number of independent points = 8.4

Samples	Abs – Sc	$N$	$R/\text{Å}$	$2\sigma^2/\text{Å}^2$	$E_0/\text{eV}$	$R_{\text{factor}}$
1 min CO	Cu–Cl (CuCl)	$1.65 \pm 0.08$	$2.21 \pm 0.01$	0.007	$-2 \pm 1$	0.005
	Cu–O (CuCl <sub>2</sub> ·2H <sub>2</sub> O)	$0.50 \pm 0.08$	$1.84 \pm 0.02$	0.003		

this. Firstly, if a mixture of Cu species is present, the coordination number obtained from the fit would only be proportional to the contributions of each species.<sup>32</sup> Secondly, destructive interference of the scattering paths from the axial and equatorial neighbours has previously been observed for distorted octahedral Cu species, resulting in only the equatorial contributions being observed, leading to difficulties in refining the coordination numbers.<sup>33</sup> As EXAFS is an averaging technique, we cannot rule out that, in our case, we may also have a mixture of Cu<sup>2+</sup> species present at this point in the reaction coordinate.

Table 2 Calculated defect formation energies for the removal of a Cl atom following eqn (4). The Cu<sub>x</sub>Cl<sub>y</sub> given in the structure definition column refers to the stoichiometric slab used for the defect calculation. Cu<sub>16</sub>Cl<sub>32</sub> is shown in Fig. 7a and Cu<sub>32</sub>Cl<sub>64</sub> is created by doubling the cell in the direction of the CuCl<sub>2</sub> chains

Structure/simulation slab	$E_{\text{def}}(U = 4)/\text{eV}$	$E_{\text{def}}(U = 7)/\text{eV}$
Surface defect/Cu <sub>16</sub> Cl <sub>32</sub>	1.23	1.32
2 <sup>nd</sup> layer defect/Cu <sub>16</sub> Cl <sub>32</sub>	1.32	1.41
Surface defect/Cu <sub>32</sub> Cl <sub>64</sub>	1.19	1.25
2 <sup>nd</sup> layer defect/Cu <sub>32</sub> Cl <sub>64</sub>	1.28	1.38



To complement these XAS measurements we have carried out electronic structure calculations on the copper chloride lattice in order to better understand the energetics and structural implications of Cl removal from the  $\text{Cu(II)Cl}_2$  lattice during heat treatment or reduction through reaction with CO. The next section covers this work and demonstrates the structural motifs that are induced on the chlorine pre-treated support that can, intermittently, support phosgene production.

### DFT results

DFT calculations began with the optimisation of the bulk unit cell lattice parameters through relaxing the atom positions for a series of cell expansion/contraction values. The resulting plot of calculated energy vs. cell volume was fitted using the Murnaghan equation of state<sup>34</sup> (Fig. S6†). The resulting bulk structure geometry gives in plane the expected  $\text{CuCl}_2$  row structures with in plane Cu–Cl distances of 2.285 Å and inter-layer axial  $\text{Cu}\cdots\text{Cl} = 3.001$  Å at the PBE+U (=7) with a D2 level of theory.

The calculated density of states with each of the two  $U$  values is shown in Fig. S7.† In both cases the band gap is defined by the top of the valence band consisting of majority spin  $\text{Cu}^{2+}$  d-states and empty d-states of the minority spin. In the case of  $U = 4$  the calculated band gap is small (0.3 eV) while for  $U = 7$  a clear gap exists of around 0.9 eV. The choice of  $U$  parameter is made so that we can demonstrate the influence of  $U$  on the calculated energies comparing the lowest value for which a band gap is present to the most commonly used value for oxidised Cu in the literature.

In our XANES data we have seen changes in oxidation state for Cu when the  $\text{Cl}_2$  pre-treated samples are subjected to a heating ramp or when CO is introduced into the system. The reduction of Cu will take place as Cl is removed from the lattice and so we have calculated the defect energies,  $E_{\text{def}}$ , for the creation of an anion vacancy in the surface. The DFT calculations also give information on the structural changes that are caused by the removal of Cl. The defect energy is calculated as the energy change for the simple reaction:



where  $m$  is the number of Cu cations present in the simulation slab. Table 2 gives the calculated energies for this process with the Hubbard  $U$  parameter set at 4 and at 7 and Fig. 7 shows the structures of the stoichiometric surface and defect structures calculated with  $U = 7$  using the  $\text{Cu}_{16}\text{Cl}_{32}$  four layer slab model. The stoichiometric surface consists of the same  $\text{CuCl}_2$  chains that were noted in the bulk (Fig. S1†). For the surface there are some small distortions of the positions of the surface Cu centres which move out of the Cl plane within the  $\text{CuCl}_2$  chains toward the centre of the slab. This reduces the axial  $\text{Cu}^{2+}\cdots\text{Cl}^-$  distance from the optimised bulk value of 3.001 Å to 2.845 Å, consistent with the loss of the second axial  $\text{Cl}^-$  ligand that these surface Cu cations experience on creation of the surface. A smaller contraction for the second layer  $\text{Cu}\cdots\text{Cl}$  (third layer) distance is also observed, with an axial separation in this case of 2.963 Å, while the Cu atom distance to  $\text{Cl}^-$  in the fourth (fixed) layer is 3.075 Å, very similar to the bulk value. The surface  $\text{Cu}\cdots\text{Cl}$  axial distance is also closer to the value measured by using EXAFS (2.86 Å, Table S1, Fig. S5†) than that for the DFT+U optimised bulk. This



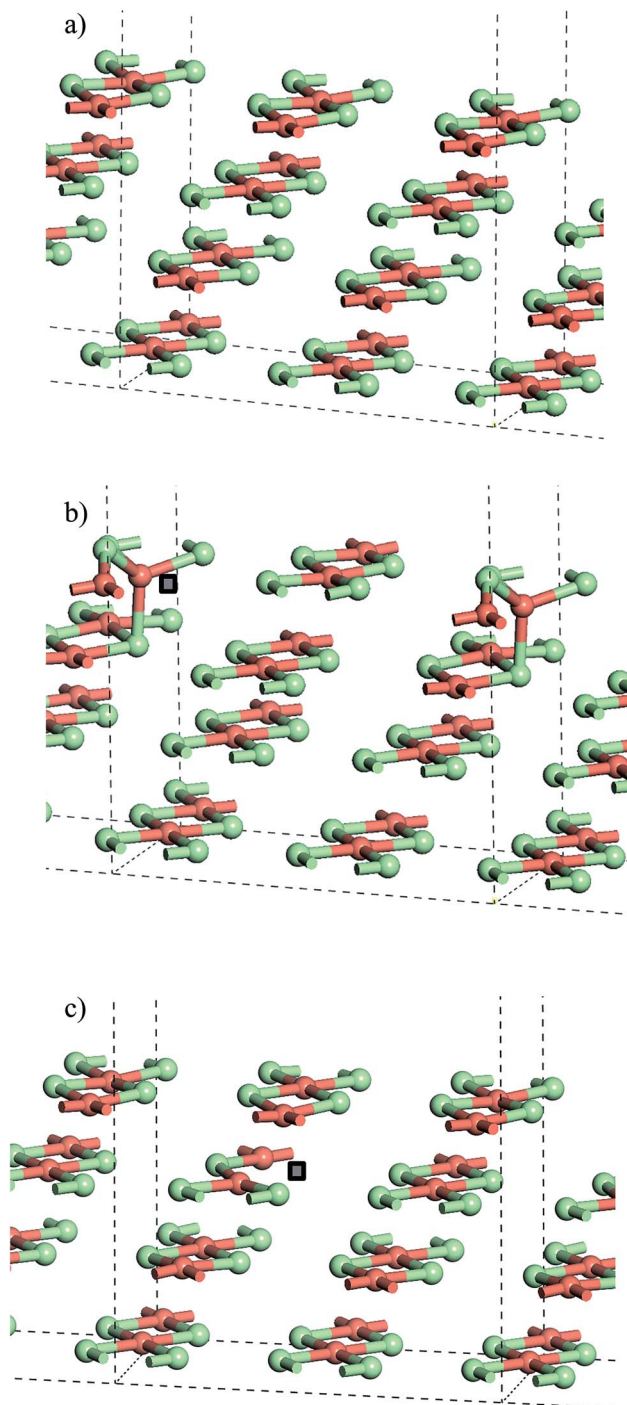


Fig. 7 (a) Slab model of the stoichiometric CuCl<sub>2</sub>(010) surface. (b) Structure with Cl<sup>-</sup> vacancy in the surface layer of the slab and (c) structure with a Cl<sup>-</sup> vacancy in the second layer of the slab. Note that the position of the anion vacancy is indicated by a grey square in (b) and (c). All structures optimised with PBE+U using  $U = 7$  and Grimme D2 dispersion included. Atoms coloured Cu: pink and Cl: green.



could suggest that the  $\text{CuCl}_2$  supported on attapulgite clay is present with a high ratio of (010) surface to bulk. For the surface layer there is also some loss of symmetry within the chains with two Cu–Cl bonds slightly longer than found in the bulk (2.296 Å *cf.* 2.285 Å) and two bonds shorter than the bulk (2.270 Å). The creation of the (010) surface only involves the removal of axial  $\text{Cu}\cdots\text{Cl}$  interactions in the strongly Jahn–Teller distorted geometry of the bulk. The calculated surface energy based on eqn (1) is correspondingly low with practically the same value obtained for  $U = 4$  or  $U = 7$  (0.121 J m<sup>-2</sup> ( $U = 4$ ) and 0.129 J m<sup>-2</sup> ( $U = 7$ )).

From the stoichiometric surface, a defect was created through the removal of a single  $\text{Cl}^-$  ion, to leave a vacancy, V, in the surface. The electron associated with this defect would be expected to reduce a single  $\text{Cu}^{2+}(\text{d}^9)$  cation to  $\text{Cu}^+(\text{d}^{10})$  and so the initial spin state arrangement used for defect calculations was adjusted to have one Cu site neighbouring the defect assigned zero spin. As the  $\text{CuCl}_4$  units are edge sharing, this results in two surface Cu ions being bridged by a single  $\text{Cl}^-$  anion. The relaxed structure (Fig. 6b) shows that the remaining  $\text{Cl}^-$  ion in the –Cu–Cl–Cu–V– square has moved out of the plane of the  $\text{CuCl}_2$  chain with one Cu cation moving closer to a second layer  $\text{Cl}^-$  ( $\text{Cu}\cdots\text{Cl}$  (2<sup>nd</sup> layer) = 2.372 Å) giving it a pseudo-tetrahedral (4-fold) geometry and one Cu cation moving further from the second layer and adopting a pseudo-trigonal planar (3-fold) geometry ( $\text{Cu}\cdots\text{Cl}$  (2<sup>nd</sup> layer) = 3.017 Å). Analysis of the final spin state shows that the 4-fold Cu has practically 0 spin while the 3-fold Cu has associated spin density. This suggests that the 4-fold Cu is formally a  $\text{Cu}^+(\text{d}^{10})$  cation while the 3-fold remains a  $\text{Cu}^{2+}(\text{d}^9)$  cation. Within the defective chain, Cu–Cl distances are also affected, with shorter Cu–Cl to the single bridging  $\text{Cl}^-$  ion than seen in the stoichiometric surface (Cu(4-fold)–Cl = 2.214 Å and Cu(3-fold)–Cl = 2.151 Å).

The calculated energy to form the surface defect in the  $\text{Cu}_{16}\text{Cl}_{32}$  slab is 1.32 eV ( $U = 7$ , Table 2) increasing to 1.41 eV if a defect is created in the second layer of the same slab model (Fig. 6c). There is very little structural re-arrangement following relaxation of the second layer defect structure compared to that discussed above for the surface defect. Hence, the higher energy to create a sub-surface defect may result from the more constrained environment of the sub-surface  $\text{Cl}^-$  sites.

Doubling the cell in the  $\text{CuCl}_2$  chain direction to give a  $\text{Cu}_{32}\text{Cl}_{64}$  slab gives a calculated surface defect energy 5% lower than calculated for the smaller cell while the second layer defect has a calculated energy around 2% lower. In the chain direction the  $\text{Cu}_{16}\text{Cl}_{32}$  cell has only two Cu sites while in the doubled cell there are four so that it should be expected, given the observed surface geometry changes, that there are defect–defect interactions present in the smaller slab. Indeed, for the surface defect model, using the larger cell, the movement of the  $\text{Cl}^-$  anion in the –Cu–Cl–Cu–V– square is significantly smaller than seen for the  $\text{Cu}_{16}\text{Cl}_{32}$  slab so that there is practically no difference in the geometries of the two Cu cations that this anion bridges (Fig. S8<sup>†</sup>). This comparison of the  $\text{Cu}_{16}\text{Cl}_{32}$  and  $\text{Cu}_{32}\text{Cl}_{64}$  slab models also suggests that at low anion defect concentrations the disruption of the lattice will be relatively minor while at high concentrations, where the  $\text{Cu}^+$  content contributes significantly to the XANES, we should also expect significant geometric changes around the Cu sites, particularly near to the surface of the  $\text{Cu}(\text{II})\text{Cl}_2$  crystallites.

Table 2 also gives data for defect creation using the  $U = 4$  Hubbard parameter which consistently gives lower calculated defect energies by between 0.06 and 0.10 eV depending on the position of the defect and the cell size employed. Even



so the differences observed between different defect locations or slab sizes follow the same trend for either choice of  $U$ , suggesting that the properties of interest here are relatively insensitive to this parameter.

Table 3 gives the calculated energies and some geometric data for the adsorption of CO to the  $\text{CuCl}_2(010)$  surface structures using the slab models for stoichiometric and defective surfaces and Fig. 8 shows the corresponding optimised geometries for the  $\text{Cu}_{16}\text{Cl}_{32}$  slab based models. CO adsorbs weakly to the stoichiometric surface with a calculated adsorption energy of only  $-13 \text{ kJ mol}^{-1}$  ( $U = 7$ ) and a relatively long  $\text{Cu}\cdots\text{CO}$  interaction distance ( $2.561 \text{ \AA}$ ), although this is still shorter than the  $\text{Cu}\cdots\text{Cl}$  distance for the inter-layer interactions in the bulk material. The  $\text{C}=\text{O}$  bond length is also close to that for the free gas phase CO reference state ( $1.143 \text{ \AA}$ ). On introduction of a surface defect the calculated CO adsorption energy becomes considerably more favourable ( $-55 \text{ kJ mol}^{-1}$ ). As discussed above the surface defect in the  $\text{Cu}_{16}\text{Cl}_{31}$  slab model is neighboured by one 4-fold and one 3-fold co-ordinated Cu centre and so we expected different behaviour for adsorption to each site. To test this two calculations were carried out and the results are compared in Table 3. The adsorption energies are actually the same irrespective of the choice of Cu site. Adsorption of CO raises the Cu site out of the surface plane producing a 4-co-ordinate Cu centre in a pseudo-tetrahedral geometry in each case (Fig. 8b and c). The Cu–CO distance is considerably shorter and the CuC–O bond length longer than seen for the stoichiometric surface, consistent with the stronger interaction with the surface. Calculation of the spin density for either structure shows practically no spin density on the Cu centre to which CO co-ordinates suggesting that the electronic state is re-organised during optimisation to place the  $\text{Cu}^+(\text{d}^{10})$  centre in the position bonding to CO (Fig. S9<sup>†</sup>) so that the surface responds to the adsorbate and re-arranges to the same structure irrespective of the initial geometry of the defect site. Although we see significant surface re-arrangement of the surface with the surface defect present the CO adsorption has a lower energy than seen for other surfaces. For example, calculations using a similar approach for CO on Fe(111) give adsorption energies of  $119 \text{ kJ mol}^{-1}$  and a  $\text{C}=\text{O}$  bond length of  $1.164 \text{ \AA}$  for CO at an Fe top site using a similar level of theory.<sup>35</sup>

**Table 3** Calculated CO adsorption energies,  $E_{\text{ads}}$ , following eqn (3). The  $\text{Cu}_x\text{Cl}_y$  given in the structure definition column refers to the slab composition.  $\text{Cu}_{16}\text{Cl}_{32}$  is shown in Fig. 7a and  $\text{Cu}_{32}\text{Cl}_{64}$  is created by doubling the cell in the direction of the  $\text{CuCl}_2$  chains. Each defect containing slab has a single Cl atom removed from the position indicated

Structure/simulation slab	$E_{\text{ads}} (U = 4)/$ $\text{kJ mol}^{-1}$	$E_{\text{ads}} (U = 7)/$ $\text{kJ mol}^{-1}$	$\text{Cu}\cdots\text{CO}^a/$ $\text{\AA}$	$\text{CuC}-\text{O}^a/$ $\text{\AA}$
Stoichiometric (010)/ $\text{Cu}_{16}\text{Cl}_{32}$	–7	–13	2.561	1.141
Surf. def., Cu(4-fold) <sup>b</sup> site/ $\text{Cu}_{16}\text{Cl}_{31}$	–55	–55	1.838	1.147
Surf. def. Cu(3-fold) <sup>b</sup> site/ $\text{Cu}_{16}\text{Cl}_{31}$	–55	–55	1.840	1.147
2 <sup>nd</sup> layer defect/ $\text{Cu}_{16}\text{Cl}_{31}$	–13	–16	2.432	1.141
Stoichiometric (010)/ $\text{Cu}_{32}\text{Cl}_{64}$	–11	–12	2.614	1.141
Surf. def./ $\text{Cu}_{32}\text{Cl}_{63}$	–39	–32	1.851	1.146
2 <sup>nd</sup> layer defect/ $\text{Cu}_{32}\text{Cl}_{63}$	–13	–15	2.417	1.140

<sup>a</sup> Geometry taken from the  $U = 7$  optimised structures. <sup>b</sup> Initial co-ordination of adsorption site in reference slab calculation.



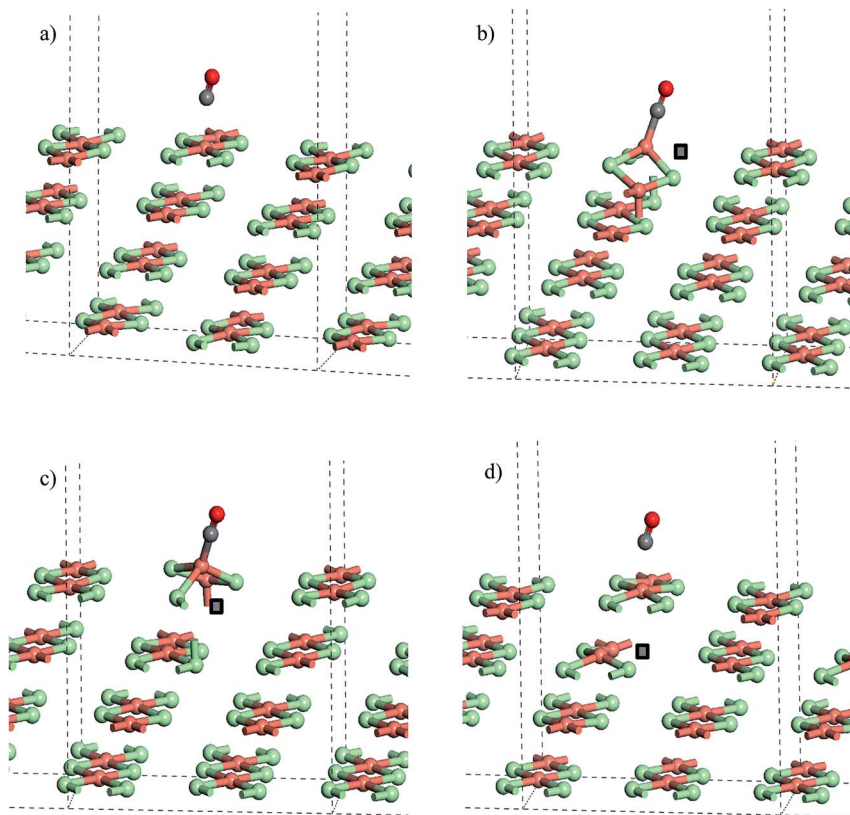


Fig. 8 Calculated CO adsorption geometries on (a) a slab model of the stoichiometric  $\text{CuCl}_2(010)$  surface. (b) Structure with  $\text{Cl}^-$  vacancy in the surface layer of a slab CO at a Cu(3-fold) site, (c)  $\text{Cl}^-$  vacancy in the surface layer with CO at a Cu(4-fold) site and (d) structure with a  $\text{Cl}^-$  vacancy in the second layer of a slab. Note that the position of the anion vacancy is indicated by a grey square in (b)–(d) the origin for cells in (b) and (c) has been shifted to place CO at the centre of the cell. All structures were optimised with PBE+U using  $U = 7$  and Grimme D2 dispersion included. Atoms coloured Cu: pink, Cl: green, C: grey, and O: red.

The strong adsorption of CO to a defect is only apparent for the  $\text{Cl}^-$  vacancy at the surface. The calculated adsorption energy for CO in the presence of a 2<sup>nd</sup> layer defect,  $-16 \text{ kJ mol}^{-1}$  ( $U = 7$ ), is close to that for the stoichiometric surface and Table 3, Fig. 8a and d also show that the calculated geometries of the adsorbed molecule are very similar.

Similar trends are seen for the larger slab model ( $\text{Cu}_{32}\text{Cl}_{64}$ ) with CO adsorption to the Cu ions close to a surface defect notably more favourable than the stoichiometric surface or adsorption with a 2<sup>nd</sup> layer defect present. Even so, the calculated energy for CO at the surface defect is lower than that found with the smaller simulation slab, suggesting that a high density of defects will favour CO uptake by the catalyst.

It can also be noted from Table 3 that the choice of the  $U$  parameter has little influence on the ordering of the calculated adsorption energies for the surface sites.





The absolute values of the adsorption energy are affected with the weaker interactions being more favourable by up to  $5 \text{ kJ mol}^{-1}$  when  $U = 7$  is used compared to  $U = 4$ .

## Conclusions

This study has examined the interaction of CO with an industrial grade  $\text{Cu(II)Cl}_2$  oxy-chlorination catalyst. CO exposure to the dried, as-received catalyst at elevated temperatures leads to the formation of  $\text{CO}_2$  as the only identifiable product, establishing a role for a CO oxidation pathway. Phosgene production could be induced through a catalyst pre-treatment where the supported  $\text{Cu(II)Cl}_2$  is exposed to a diluted stream of chlorine. Subsequent CO exposure at  $\sim 370^\circ\text{C}$  then leads to phosgene production. From X-ray absorption data supported by DFT calculations the following conclusions can be drawn.

- XANES shows a pre-chlorination step modifies the as-received  $\text{Cu(II)Cl}_2$  catalyst so that it more closely resembles anhydrous  $\text{Cu(II)Cl}_2$ .

- On heating the as-received and chlorine pre-treated catalysts in an inert atmosphere up to  $367^\circ\text{C}$ , a temperature where phosgene formation is observed, XANES shows the samples to be comprised of a mixture of  $\text{Cu}^+$  and a small amount of  $\text{Cu}^{2+}$ .

- XANES shows elevated temperature CO exposure to the untreated catalyst leads to no noticeable change in the copper oxidation state. However, for the pre-treated catalyst an oxidation of  $\text{Cu}^+ \rightarrow \text{Cu}^{2+}$  is observed in the first minute of CO exposure. On continued exposure of CO, the XANES spectrum shows reduction and a return to the  $\text{Cu}^+$  species. It is tentatively proposed that the short-lived oxidation process occurs as a consequence of CO induced release of  $\text{Cl}_2$  from the catalyst pore network.

- In conjunction with EXAFS measurements, DFT calculations have modelled the surface structure of copper chloride particles, respecting the Jahn–Teller distorted geometry of the bulk, and including a role for  $\text{Cl}^-$  defect sites that will be created as the Cu oxidation state changes and phosgene is produced.

- Calculated CO adsorption energies show that CO binds more strongly in the presence of a surface defect with CO adsorbing at the associated  $\text{Cu}^+$  site. This suggests that a mixed  $\text{Cu}^+/\text{Cu}^{2+}$  catalyst is required to support CO chemisorption and subsequent chlorination in order to produce phosgene molecules.

## Acknowledgements

The UK Catalysis Hub is kindly thanked for resources and support provided *via* our membership of the UK Catalysis Hub Consortium and funded by EPSRC (grants EP/I038748/1, EP/I019693/1, EP/K014706/1, EP/K014668/1, EP/K014854/1, EP/K014714/1 and EP/M013219/1). *Via* our membership of the UK's HPC Materials Chemistry Consortium, which is funded by EPSRC (EP/L000202), this work made use of the facilities of ARCHER. Computing resource was also provided by Advanced Research Computing at Cardiff (ARCCA) and the HPC-Wales supercomputer facilities. We acknowledge Diamond Light Source for beamtime through award SP10306, and thank the beamline scientists Dr Diego Gianolio and Dr Giannantonio Cibin. Ineos Chlor is thanked for the provision of the  $\text{Cu(II)Cl}_2$  catalyst. The data used to generate the results presented in this paper is available at: <http://doi.org/10.17035/d.2018.0045168390>.



## References

- 1 E. K. Gibson, J. M. Winfield, K. W. Muir, R. H. Carr, A. Eaglesham, A. Gavezzotti and D. Lennon, *Phys. Chem. Chem. Phys.*, 2010, **12**, 3824.
- 2 F. Calvini, *Catal. Today*, 2010, **157**, 8.
- 3 T. Zhang, C. Troll, B. Rieger, J. Kintrup, O. F.-K. Schluter and R. Weber, *Appl. Catal., A*, 2009, **357**, 51.
- 4 T. Zhang, C. Troll, B. Rieger, J. Kintrup, O. F.-K. Schluter and R. Weber, *Appl. Catal., A*, 2009, **365**, 20.
- 5 T. Zhang, C. Troll, B. Rieger, J. Kintrup, O. F.-K. Schluter and R. Weber, *J. Catal.*, 2010, **270**, 76.
- 6 I. W. Sutherland, N. G. Hamilton, C. C. Dudman, P. Jones, D. Lennon and J. M. Winfield, *Appl. Catal., A*, 2011, **399**, 1.
- 7 I. W. Sutherland, N. G. Hamilton, C. C. Dudman, P. Jones, D. Lennon and J. M. Winfield, *Appl. Catal., A*, 2014, **471**, 149.
- 8 J.-B. d'Espinose de la Caillerie and J. J. Fripiat, *Clays Clay Miner.*, 1992, **40**, 457.
- 9 M. Suárez and E. García-Romero, *Appl. Clay Sci.*, 2006, **31**, 154.
- 10 N. B. Muddada, U. Olsbye, L. Caccialupi, F. Cavani, G. Leofanti, D. Gianolio, S. Bordiga and C. Lamberti, *Phys. Chem. Chem. Phys.*, 2010, **12**, 5605.
- 11 C. Lamberti, C. Prestipino, F. Bonino, L. Capello, S. Bordiga, G. Spoto, A. Zecchina, S. D. Moreno, B. Cremaschi, M. Garilli, A. Marsella, D. Carmello, S. Vidotto and G. Leofanti, *Angew. Chem., Int. Ed.*, 2002, **41**, 2341.
- 12 G. Leofanti, M. Padovan, M. Garilli, D. Carmello, A. Zecchina, G. Spoto, S. Bordiga, G. Turnes Palomino and C. Lamberti, *J. Catal.*, 2000, **189**, 91.
- 13 G. Leofanti, A. Marsella, B. Cremaschi, M. Garilli, A. Zecchina, G. Spoto, S. Bordiga, P. Fiscaro, G. Berlier, C. Prestipino, G. Casali and C. Lamberti, *J. Catal.*, 2001, **202**, 279.
- 14 N. B. Muddada, U. Olsbye, L. Caccialupi, F. Cavani, G. Leofanti, D. Gianolio, S. Bordiga and C. Lamberti, *Phys. Chem. Chem. Phys.*, 2010, **12**, 5605.
- 15 S. Guan, G. E. Rossi, D. Lennon, P. R. Davies, D. J. Willock, J. M. Winfield and C. Wilson, in preparation.
- 16 S. Lebernegg, M. Schmitt, A. A. Tsirlin, O. Janson and H. Rosner, *Phys. Rev. B: Condens. Matter Mater. Phys.*, 2013, **87**, 155111.
- 17 M. Ferrandon, V. Daggupati, Z. Wang, G. Naterer and L. Trevani, *J. Therm. Anal. Calorim.*, 2015, **119**, 975.
- 18 M. Newville, *J. Synchrotron Radiat.*, 2001, **8**, 322.
- 19 B. Ravel and M. Newville, *J. Synchrotron Radiat.*, 2005, **12**, 537.
- 20 G. Malta, S. A. Kondrat, S. J. Freakley, C. J. Davies, L. Lu, S. Dawson, A. Thetford, E. K. Gibson, D. J. Morgan, W. Jones, P. P. Wells, P. Johnston, C. R. A. Catlow, C. J. Kiely and G. J. Hutchings, *Science*, 2017, **355**, 1399.
- 21 G. Kresse and J. Furthmüller, *Phys. Rev. B: Condens. Matter Mater. Phys.*, 1996, **54**, 11169–11186; G. Kresse and J. Hafner, *Phys. Rev. B: Condens. Matter Mater. Phys.*, 1993, **47**, 558.
- 22 J. P. Perdew, S. Burke and M. Ernzerhof, *Phys. Rev. Lett.*, 1996, **77**, 3865.
- 23 P. E. Blöchl, *Phys. Rev. B: Condens. Matter Mater. Phys.*, 1994, **50**, 17953; G. Kresse and J. Joubert, *Phys. Rev. B: Condens. Matter Mater. Phys.*, 1999, **59**, 1758.
- 24 S. Grimme, *J. Comput. Chem.*, 2006, **27**, 1787.



- 25 H. J. Monkhorst and J. D. Pack, *Phys. Rev. B: Solid State*, 1976, **13**, 5188.
- 26 S. L. Dudarev, G. A. Botton, S. Y. Savrasov, C. J. Humphreys and A. P. Sutton, *Phys. Rev. B: Condens. Matter Mater. Phys.*, 1998, **57**, 1505.
- 27 D. O. Scanlon, B. J. Morgan and G. W. Watson, *J. Chem. Phys.*, 2009, **131**, 124703.
- 28 A. K. Mishra, A. Roldan and N. H. de Leeuw, *J. Phys. Chem. C*, 2016, **120**, 2198.
- 29 K. L. Howard and D. J. Willock, *Faraday Discuss.*, 2011, **152**, 135.
- 30 A. J. Berry, A. C. Hack, J. A. Mavrogenes, M. Newville and S. R. Sutton, *Am. Mineral.*, 2006, **91**, 1773.
- 31 L.-S. Kau, D. J. Spira-Solomon, J. E. Penner-Hahn, K. O. Hodgson and E. I. Solomon, *J. Am. Chem. Soc.*, 1987, **109**, 6433.
- 32 C. Lamberti, C. Prestipino, L. Capello, S. Bordiga, A. Zecchina, G. Spoto, S. Diaz Moreno, A. Marsella, B. Cremaschi, M. Garilli, S. Vidotto and G. Leofanti, *Int. J. Mol. Sci.*, 2001, **2**, 230.
- 33 K. Kervinen, P. C. A. Bruijninx, A. M. Beale, J. Gerbrand Mesu, G. van Koten, R. J. M. Klein Gebbink and B. M. Weckhuysen, *J. Am. Chem. Soc.*, 2006, **128**, 3208.
- 34 F. D. Murnaghan, *Proc. Natl. Acad. Sci. U. S. A.*, 1944, **30**, 244.
- 35 S. Booyens, M. Bowker and D. J. Willock, *Surf. Sci.*, 2014, **625**, 69.

